c-Maf and Mafb function combinatorially to establish SGN subtype-specific synaptic properties

Isle Bastille[1], Lucy Lee[1], Cynthia Moncada-Reid[1], Wei-Ming Yu[2], Austen Sitko[1], Andrea Yung[3], and Lisa Goodrich[1,*]

[1]Department of Neurobiology, Harvard Medical School, Boston, MA
[2]Department of Biology, Loyola University Chicago, Chicago, IL
[3]Genentech, South San Francisco, CA
* Corresponding author

Abstract:
Diverse types of synapses transmit the vast information encoded in the nervous system. Even neurons of the same type can exhibit synaptic heterogeneity that alters circuit output. For instance, in the auditory system, each inner hair cell (IHC) signals to multiple Type I spiral ganglion neurons (SGNs) via glutamatergic synapses with heterogeneous properties, thereby communicating information about the frequency, timing, and intensity of the sounds we hear. Type I SGNs fall into three molecularly distinct subtypes (Ia, Ib and Ic) that make synapses with predictable differences in the position and volume of the glutamate receptor puncta, as well as the size of the apposing pre-synaptic ribbon in the IHC. To define the intrinsic mechanisms that determine subtype-appropriate synaptic properties, we investigated Maf family transcription factors, which play known roles in synapse development. Loss of *c-Maf* or *Mafb* from SGNs led to opposing effects on synaptic morphology and auditory responses, whereas loss of both *c-Maf* and *Mafb* led to formation of dysmorphic synapses and abnormal auditory responses. Further, although *c-Maf* and *Mafb* are both expressed in all SGNs, their levels differ across SGN subtypes. Single-cell RNA sequencing of single mutant SGNs revealed that c-Maf and Mafb have both shared and unique effects on subtype-specific programs of gene expression, including molecules associated with synaptic function and neuronal excitability. Double mutant SGNs, on the other hand, failed to diversify and showed dramatic changes in gene expression that included genes not changed in either single mutant. Together, these findings suggest that a combinatorial code of c-Maf and Mafb acts across SGN subtypes to establish synaptic heterogeneity that is critical for normal hearing function.

Introduction:
Robust and accurate synaptic transmission is essential for perception and behavior. The task of relaying a huge range of sensory information is divided into sensory neuron subpopulations that each encode distinct features of incoming stimuli. To this end, sensory neuron synapses differ widely in their composition, size, and morphology, thereby enabling finely tuned differences in their signaling properties (Petitpré et al., 2022). This large range of synaptic features is in part dictated and maintained by the distinct transcriptional instructions found in each neuronal subtype. Although many synaptic proteins have been identified and characterized for their effects on signal transmission, it is unclear how groups of proteins are co-regulated to achieve appropriate cell-type specific synaptic properties.

In the periphery of the auditory system, Type I spiral ganglion neurons (SGNs) relay complex sound information from mechanosensitive inner hair cells (IHC) to the brain via highly

specialized ribbon synapses (Shrestha and Goodrich, 2019). Presynaptic densities, known as ribbons, localize to the basolateral pole of the IHC and cluster synaptic vesicles that release glutamate onto receptors in SGN postsynaptic densities. Sound frequency is encoded topographically, with SGNs in the apex of the cochlea responding to lower frequency sounds and SGNs in the base responding to higher frequencies. Most SGNs receive input from one IHC and each IHC signals to approximately 10-20 SGNs depending on tonotopic location (Perkins and Morest, 1975; Ryugo, 1992; Spoendlin, 1985). At any one position, sound intensity is captured by an action potential rate code, with louder sounds eliciting more spikes. A single SGN is best tuned to a certain frequency and can only encode information about a small proportion of the range of sound intensities found in the environment. However, as a population, SGNs can tile a huge dynamic range of frequencies and intensities with high fidelity and speed.

Although IHC-SGN synapses are uniformly glutamatergic, Type I SGNs exhibit stereotyped differences in their physiological and synaptic properties that shape how sound information is communicated to the central nervous system (Shrestha and Goodrich, 2019). At the physiological level, Type I SGNs exhibit different thresholds and spontaneous firing rates (SR) that allow them to capture the complete range of sound intensities found in the environment (Kiang, 1965; Liberman, 1982). Some of this functional diversity likely reflects intrinsic differences among the Type I SGNs. There are three molecularly defined subtypes of Type I SGNs, known as the Ia, Ib, and Ic subtypes, that differ in expression of many transcription factors and synaptic genes (Petitpré et al., 2018; Shrestha et al., 2018; Sun et al., 2018). Ia, Ib, and Ic SGNs match the anatomical features of the physiologically defined subtypes, exemplified by the orderly arrangement of their terminals along the basolateral surface of the IHC, with Ia SGN terminals in the same position as high SR SGNs, Ic SGN terminals in the low SR SGN position, and Ib SGNs in the middle, where medium SR SGN terminals reside (Shrestha et al., 2018). Likewise, genetically labeled Ic SGNs consistently exhibit low spontaneous firing rates when recorded from *in vitro* (Siebald et al., 2023). On the other hand, genetically labeled Ia and Ib SGNs show extensive variability in their firing rates (Siebald et al., 2023), possibly due to differences in their local connectivity. Indeed, individual IHC-SGN synaptic compositions show extensive heterogeneity in composition, size, and morphology (Hu et al., 2020; Liberman et al., 2011; Liberman and Liberman, 2016; Michanski et al., 2019; Payne et al., 2021). Some of these differences are linked to subtype identity. For instance, Type Ia SGNs make synapses with larger ribbons and smaller GluA2 puncta than the Type Ib and Ic SGNs, again correlating with previously described electrophysiological subtypes (Shrestha et al., 2018). This suggests that synaptic diversity in SGNs is in part dictated by distinct transcriptional networks and contributes to differences in their functional output. By identifying and analyzing transcription factors that impart subtype-specific differences in synaptic properties, we can better understand how intrinsic differences in subtype identity influence sensory neuron functional diversification.

SGNs develop from neuronal progenitors in the otocyst and acquire their mature identities through the sequential activity of transcription factors (Goodrich, 2016). First, Gata3 guides neuronal progenitors towards an auditory fate and promotes their differentiation, including guidance of peripheral processes towards the hair cell (Appler et al., 2013). As differentiation progresses, SGNs begin to produce Mafb, which acts downstream of Gata3 and is required for the formation of functional synapses (Yu et al., 2013). Meanwhile, Runx1 guides

the proper specification and maintenance of SGN subtype identity. Removing *Runx1* results in the depletion of Ib and Ic identities in favor of Ia SGNs (Shrestha et al., 2023). This shift in identity results in a corresponding shift in synaptic properties, with more neurons forming Ia-like synapses. Thus, in *Runx1* conditional knock-out mice, postsynaptic glutamate receptor clusters on the modiolar side of the IHC, i.e. where Ib and Ic SGNs normally form synapses, are larger in size, matching the cluster sizes normally seen among Ia synapses. The formation of synapses with both cell-type specific and variable properties seems to involve dynamic changes in the position, shape, and size of pre- and post-synaptic elements that begin around birth and continue through the first month of life. The final pattern is shaped by thyroid hormone signaling and is maintained by inputs from the olivocochlear efferent system (Coate et al., 2019; Sendin et al., 2007; Yin et al., 2014). However, the transcriptional programs that determine SGN subtype-specific synaptic properties are unknown.

The basic leucine zipper transcription factors c-Maf and Mafb are excellent candidates for regulation of SGN synaptic features. In other systems, Maf family members control terminal cell differentiation by inducing and maintaining identity-specific features such as the production of glucagon by pancreatic cells (Yang and Cvekl, 2016). Deletion of *Mafb* from SGNs in mice disrupted development of the postsynaptic density, resulting in reduced ABR responses (Yu et al., 2013). However, many functional synapses remained, raising the possibility of compensation by another family member. Like *Mafb*, *c-Maf* is expressed downstream of Gata3 in SGNs, but its role has not been determined (Appler et al., 2013; Yu et al., 2013). Work in the somatosensory system demonstrated that c-Maf is essential for the development of vibration-sensitive neurons, acting in part by regulation of ion channels needed for mature function (Wende et al., 2012). In addition, cultured cortical interneurons from *c-Maf* knockout animals form more synapses, while those from *Mafb* knockouts form fewer, echoing Mafb's role in SGNs and emphasizing the possibility that c-Maf and Mafb have independent effects (Pai et al., 2019). c-Maf and Mafb can act cooperatively through dimerization with each other and with other transcription factors (Pogenberg et al., 2014; Rodríguez-Martínez et al., 2017; Suda et al., 2014; Yang and Cvekl, 2016). Therefore, combinations of c-Maf and Mafb could elicit a variety of differentiation programs, including genes needed to make diverse synapses.

In this study, we investigated the role of c-Maf and Mafb in the establishment of SGN peripheral synaptic properties. Analysis of anatomical and functional phenotypes as well as gene expression changes in single and double conditional knock-out mice suggests that a different combination of Maf effectors acts in each SGN subtype to generate diversity, including the acquisition of subtype-appropriate synaptic properties.

Results:

Given the nature of the previously described *Mafb* phenotype (Yu et al., 2013) and the evidence that c-Maf and Mafb both influence cortical interneuron synapse number (Pai et al., 2019), we hypothesized that Mafb and c-Maf work together to regulate SGN synaptic development and function. To identify both independent and compensatory roles, we stained for pre- and postsynaptic proteins in *c-Maf* and *Mafb* mutant mice made using the same Cre driver. The *bhlhe22*^{Cre} driver was crossed to *c-Maf*$^{flox/flox}$;*Mafb*$^{flox/flox}$ mice to generate c-Maf/Mafb conditional double knockout mice (cDKO, *bhlhe22*$^{Cre/+}$;*c-Maf*$^{flox/flox}$;*Mafb*$^{flox/flox}$, N=10). In the inner ear, *bhlhe22*^{Cre} is exclusively active in neurons (Druckenbrod and Goodrich, 2015; Ross et al.,

2010). Although *bhlhe22*^{Cre} also mediates recombination in olivocochlear efferents (Appler et al., 2013), neither *c-Maf* nor *Mafb* is detected in these neurons (Frank et al., 2023) (**Figure S1**). This cross also generated knockouts for c-Maf (*c-Maf*^{cKO}, *bhlhe22*$^{Cre/+}$*;c-Maf*$^{flox/flox}$*;Mafb*$^{flox/+}$*,* N=9*)* and Mafb (*Mafb*^{cKO}, *bhlhe22*$^{Cre/+}$*;c-Maf*$^{flox/+}$*;Mafb*$^{flox/flox}$, N=7*)* as well as control animals (NoCre, *c-Maf*$^{flox/flox}$;*Mafb*$^{flox/flox}$, N=15), which allowed us to analyze the relative contributions of these two transcription factors as well as the effects of the combined loss of both within the same cross. Analysis of the overall wiring of the cochlea revealed disorganized innervation of outer hair cells by Type II SGNs (**Figure S1**) but no obvious change in the number or position of Type I SGNs or of the organization of their peripheral processes. We therefore proceeded to assess synaptic heterogeneity among Type I SGNs by staining wholemount cochlea preparations for CTBP2 and GluA2 to visualize presynaptic ribbons and postsynaptic glutamate receptor puncta, respectively.

Qualitatively, synapses were highly abnormal in the cDKO cochlea, whereas the single mutants exhibited subtle yet complementary changes in synaptic morphology. In cDKOs, the synaptic puncta appeared more variable in size and distribution than in controls, with aggregates of small and large synaptic puncta (**Figure 1A**). In the single mutants, postsynaptic GluA2 puncta appeared larger in c-Maf^{cKO} cochleae and smaller in Mafb^{cKO} cochleae compared to controls. To understand the relative contributions of c-Maf and Mafb, we created reconstructions of synaptic puncta in the 16 kHz region of control (NoCre), c-Maf^{cKO}, Mafb^{cKO}, and cDKO cochleae. This is the region of highest frequency sensitivity in mice and accordingly has the most synaptic puncta (Meyer et al., 2009). To account for any technical differences across experiments, we normalized volume measurements by the median of the control values within each batch. Quantification confirmed antagonistic effects on synaptic puncta volume in c-Maf^{cKO} and Mafb^{cKO} mice. As in controls, puncta volumes ranged widely in each single mutant strain. However, this distribution was shifted significantly towards larger GluA2 puncta volumes in c-Maf^{cKO} mice (Kruskal-Wallis with Bonferroni adjusted posthoc-Dunn, p=2.85E-23) and towards smaller volumes in Mafb^{cKO} mice (Kruskal-Wallis with Bonferroni adjusted posthoc-Dunn, p=4.17E-02) compared to controls (**Figure 1B**). Median volumes also trended in opposite directions, with median GluA2 volumes in c-Maf^{cKO} mice significantly larger than those in Mafb^{cKO} mice (**Figure 1C**) (Kruskal-Wallis with Bonferroni adjusted posthoc-Dunn, p=0.033). Although median punctum volume in c-Maf^{cKO} mice showed a trend to be larger and Mafb^{cKO} mice showed a trend to be smaller, there was no statistically significant difference for either strain compared to littermate controls (Kruskal-Wallis test with Bonferroni adjusted posthoc-Dunn, $p_{cMafcKO}$=0.100, $p_{MafbcKO}$=1.00), likely due to the high degree of variability in each genotype. Median GluA2 punctum volume was also not significantly different in cDKO animals compared with controls (Kruskal-Wallis with Bonferroni adjusted posthoc-Dunn, p=1.00), possibly due to the presence of both very small and very large puncta in the aggregates that formed. Similar effects were observed in the 8kHz region of the cochlea (data not shown). Although the *c-Maf*^{cKO} and *Mafb*^{cKO} mutants were also heterozygous for the other Maf factor, the same basic phenotypes were observed in true single knockouts, i.e. *bhlhe22*$^{Cre/+}$*;c-Maf*$^{flox/flox}$ and *bhlhe22*$^{Cre/+}$*;c-Maf*$^{flox/GFP}$ mice (**Figure S1** and (Yu et al., 2013)).

Consistent with qualitative observations, the distribution of puncta volumes is broader in cDKO animals (**Figure 1B**). Accordingly, the distribution of GluA2 volumes in cDKO animals had a larger interquartile range than in controls (Kruskal-Wallis with Bonferroni adjusted

posthoc-Dunn, p=0.034). Given the opposing effects of c-Maf and Mafb on punctum volume, the larger variance in volumes could be caused by dysregulation of synaptic properties that are normally controlled independently by each Maf factor. In fact, c-Maf^{cKO} (Kruskal-Wallis with Bonferroni adjusted posthoc-Dunn, p=0.014) and Mafb^{cKO} animals (Kruskal-Wallis with Bonferroni adjusted posthoc-Dunn, p=0.003) had larger interquartile ranges compared to control animals (**Figure 1D**). Taken together, these data indicate that GluA2 puncta become larger in c-Maf^{CKO} mice and smaller in Mafb^{CKO} mice, with both larger and smaller puncta in cDKO animals (arrows, **Figure 1A**). In cDKO animals, the presence of more very small puncta is balanced by the presence of more very large puncta, resulting in no change in the median punctum volume per hair cell per animal (**Figure 1C**). The same differences were observed in unnormalized data (**Figure S1**).

Another striking feature of the cDKO phenotype is the abnormal distribution of synaptic puncta along the bottom of the hair cell. Qualitatively, the puncta appeared to be less evenly spread out, clustering towards the center of the IHC's basal pole. Consistent with this assessment, inter-punctum distances, i.e. the closest distance of each punctum to another punctum, were significantly smaller in cDKO animals compared to controls (Kruskal-Wallis with Bonferroni adjusted posthoc-Dunn, p=2.17E–4). The inter-punctum distances were not changed in Mafb^{cKO} or c-Maf^{cKO} animals relative to controls (Kruskal-Wallis with Bonferroni adjusted posthoc-Dunn, p=1.00 for both comparisons) (**Figure 1E**). Collectively, these studies demonstrate that cDKO animals have severe synaptic phenotypes that are different from what is observed in either single mutant.

Altered auditory sensitivity in *c-Maf* and *Mafb* mutants

Glutamaterigic signaling at ribbon synapses is necessary for transmitting auditory information from IHCs to SGNs. To test if the synaptic effects observed in c-Maf and *Mafb* mutants have functional consequences for auditory sensitivity, we recorded auditory brainstem responses (ABRs) from control, single, and double knockout mice. ABRs are recorded by placing electrodes near the base of the skull of anesthetized mice to measure electric field potentials generated by synchronous firing of neurons at different steps along the ascending auditory pathway in response to sound stimuli. We presented pure tone bursts of 8,16, 32, and 45 kHz each at increasing sound pressure levels from 20 to 90 dB SPL (decibels sound pressure level) in 5 dB increments to control (*c-Maf$^{flox/flox}$;Mafb$^{flox/flox}$,* N=14), *c-Maf* knockout (*bhlhe22$^{Cre/+}$;c-Maf$^{flox/flox}$;Mafb$^{flox/+}$*, N=6), *Mafb* knockout (*bhlhe22$^{Cre/+}$;c-Maf$^{flox/+}$;Mafb$^{flox/flox}$,* N=11), and double knockout (*bhlhe22$^{Cre/+}$;c-Maf$^{flox/flox}$;Mafb$^{flox/flox}$,* N=9) littermates. There were no significant differences in distortion product otoacoustic emissions (DPOAE) thresholds across genotypes (16kHz, Kruskall-Wallis, p=0.115) (**Figure S2**). Since DPOAE are indicators of outer hair cell function, these results suggested that the observed changes in ABRs originate with IHC, SGNs, or the synapses that link them. Qualitatively, the ABR peaks seemed larger in amplitude in c-Maf^{cKO} animals, smaller in Mafb^{cKO} animals, and nearly undetectable for most sound pressure levels in the cDKO animals (**Figure 2A-D**). Auditory sensitivity is measured by identifying the lowest sound pressure level, or threshold, that elicits a brainstem response at each frequency. We only analyzed the ABR responses to 8 and 16 kHz stimuli to avoid confounds of high frequency hearing loss characteristic of certain strains of mice (Kane et al., 2012); indeed, the ABR threshold was elevated for control animals beyond 32 kHz (**Figure 2E**). We also measured

the amplitude and latency of the first peak of the ABR response (P1) which corresponds to the degree and speed of synchronous firing of SGNs (Melcher and Kiang, 1996).

Consistent with the observed synaptic defects, loss of *c-Maf* or *Mafb* had different effects on ABR thresholds and strength of synchronous SGN firing. There were significant changes in both threshold, P1 amplitude, and P1 latency across groups for most sound pressure levels (statistical comparisons in **Supplemental Table 1**). Corroborating previous findings (Yu et al., 2013), Mafb^{cKO} animals had significantly elevated thresholds at 16kHz (Kruskal-Wallis with Bonferroni adjusted posthoc-Dunn, p=0.0355), significantly smaller P1 amplitudes, and delayed latencies compared to controls (**Figure 2E-G**, **Figure S2**). By contrast, c-Maf^{cKO} animals showed no threshold shifts (Kruskal-Wallis with Bonferroni adjusted posthoc-Dunn, p=0.240). However, P1 occurred significantly later and trended towards larger amplitudes compared to controls (**Figure 2E-G**, **Figure S2**). cDKO animals had significantly elevated thresholds (Kruskal-Wallis with Bonferroni adjusted posthoc-Dunn, p=1.140E-4) and decreased P1 amplitudes compared to all the other genotypes (**Figure 2E-G**). We did not measure latency in cDKO animals since it was difficult to reliably identify P1 in these highly aberrant ABRs. The exacerbated effects on threshold and P1 amplitudes in cDKO animals suggest that *c-Maf* and *Mafb* act synergistically to control SGN properties needed for synchronous firing. In support of this idea, cDKO animals also exhibited higher thresholds and lower P1 amplitudes than Mafb^{cKO} animals. Since the only difference between Mafb^{cKO} animals (*bhlhe22$^{Cre/+}$;Mafb$^{flox/flox}$;c-Maf$^{flox/+}$*) and cDKO littermates (*bhlhe22$^{Cre/+}$;Mafb$^{flox/flox}$;c-Maf$^{flox/flox}$)* was a single copy of *c-Maf,* this result confirms a critical role for c-Maf, despite the relatively mild phenotypes observed in single c-Maf^{cKO} mice*.* Notably, the ABRs matched predictions from the observed synaptic defects, with smaller responses and smaller GluA2 puncta in Mafb^{cKO}s *vs.* slightly larger responses and larger GluA2 puncta in c-Maf^{cKO}s. Further, by comparison to the single mutants, cDKO animals showed more severe synaptic defects and accordingly poor auditory responses. Thus, Mafb and c-Maf seem to have both independent and combinatorial effects on SGN synaptic differentiation and function.

Complementary expression patterns of c-Maf and Mafb across SGN subtypes

SGN molecular subtypes express both shared and distinct synaptic genes, including postsynaptic receptors, synaptic adhesion molecules, and potassium, sodium and calcium channels (Petitpré et al., 2018; Shrestha et al., 2018; Sun et al., 2018). However, the transcriptional determinants that drive subtype-specific differences in synaptic gene expression are unknown. The opposing effects seen in the single mutants together with the exacerbated phenotypes in double mutants raised the possibility that c-Maf and Mafb influence subtype-specific programs for synaptic differentiation. In support of this idea, re-analysis of published single cell RNA sequencing (scRNA-seq) datasets showed that there are more *c-Maf* transcripts in Ia SGNs, which express the Ia-enriched gene *Rxrg*, and more *Mafb* transcripts in Ib and Ic SGNs, which express the Ib/Ic-enriched gene *Netring1* (Petitpré et al., 2022; Shrestha et al., 2018) (**Figure 3A-B**). We confirmed differential expression of c-Maf at the protein level across SGN subtypes by double staining for c-Maf and Calb2 in cochlear sections from P27-P30 mice (N=3) (**Figure 3C**). Quantification of staining intensity in 3D reconstructions of individual SGNs showed that c-Maf staining intensity correlated positively with Calb2 staining intensity (R=0.550, p=1.818E-24) (**Figure 3D**). Thus, at both the RNA and protein levels, c-Maf is higher in Ia SGNs

than in Ib and Ic SGNs. We were unable to measure adult Mafb protein expression because Mafb protein exits the nucleus after the first postnatal week and the antibody available is not sensitive enough to make quantitative assessments.

Further analysis demonstrated that c-Maf and Mafb are also expressed differentially across SGN subtypes during synaptogenesis, which occurs during the first two postnatal weeks of life in mice (Coate et al., 2019; Huang et al., 2012; Yu and Goodrich, 2014). To mark developing SGN subtypes definitively, we used *NetrinG1*$^{Cre/+}$, which mediates recombination of the Ai14 reporter only in adult Ib and Ic subtypes, consistent with its scRNA-seq expression profile (**Figure 3B**). This activity begins postnatally, with a sparse subset of SGNs expressing tdTomato in postnatal day 6 (P6) *NetrinG1*$^{Cre/+}$*;Ai14/+* mice. Since we find nearly complete coverage of Ib and Ic SGNs in adult *NetrinG1*$^{Cre/+}$*;Ai14/+* mice (Kreeger, Copeland, and Goodrich, ARO abstract, 2022), any tdTomato labeling at P6 is a reliable indication of a Ib or Ic identity. Although *NetrinG1*$^{Cre/+}$ also drives recombination in a subset of myelinating glia at this stage, these cells are readily distinguishable from neurons by the smaller size of their cell bodies, more intense tdTomato expression, and fried-egg-like morphologies (**Figure 3E**). c-Maf and Mafb levels were quantified by measuring mean staining intensities in 3D reconstructions of individual tdTomato+ (Ib/Ic) and tdTomato- (undetermined identity) SGN cell bodies in P6 *NetrinG1*$^{Cre/+}$*;Ai14/+* mice (N=5) (**Figure 3E,G**). To account for any technical differences in staining intensity across experiments, we standardized (z-scored) the staining intensity for cells in each animal so that the mean staining intensity for each animal is 0 and the standard deviation across cells is 1. Consistent with what was observed at the RNA level in adults (**Figure 3A-B**), developing tdTomato+ Ib and Ic SGNs had lower c-Maf staining intensity (Mann Whitney Rank Sum, statistic=32117.0, p=1.934E-14) (**Figure 3 E,F**) and higher Mafb staining intensity (Mann Whitney Rank Sum, statistic=6923.0, p=4.701E-16) (**Figure 3G,H**) than tdTomato- cells. These results suggest that c-Maf and Mafb are already expressed at different levels in SGN subtypes during peak synaptogenesis (Coate et al., 2019; Huang et al., 2012; Yu and Goodrich, 2014). Transcriptomes from P3 SGNs show enrichment of *c-Maf* in developing Ia SGNs whereas *Mafb* was expressed at similar levels in all SGNs at this stage (Petitpré et al., 2018), suggesting that the adult pattern of expression emerges as identities are consolidating concomitant with synaptic differentiation. Thus, *c-Maf* and *Mafb* could be playing distinct roles in regulating gene expression needed for subtype-specific features of the synapse.

Emergent gene expression changes and defects in subtype diversification in cDKOs

The constellation of phenotypes observed in single and double mutants is consistent with regulation by combinations of Mafb and c-Maf that have complex effects on gene expression. To assess gene expression changes conferred by Mafb and c-Maf alone or together, we compared the transcriptomes of SGNs from *c-Maf* and *Mafb* single and double knockout mice and littermate controls. In these experiments, true single mutants were used, thereby allowing us to confidently attribute gene expression changes to the loss of c-Maf, Mafb, or both c-Maf and Mafb. True single mutants refer to animals where one Maf factor was knocked and which contain both copies of the other Maf factor. In control transcriptomes, SGNs segregated into the three expected Ia, Ib, and Ic clusters, as identified by previously defined marker genes. As expected, *c-Maf* and *Mafb* were expressed at different levels across SGN subtypes, with more *c-Maf* in Ia SGNs and more *Mafb* in Ib and Ic SGNs (**Figure 4A**).

Analysis of single mutant transcriptomes confirmed independent roles for *c-Maf* and *Mafb* in Ia, Ib, and Ic SGN subtypes. We performed unsupervised clustering analysis on c-Maf^{cKO} (*bhlhe22*$^{Cre/+}$*;c-Maf*$^{fl/fl}$, N=3 mice, n= 1708 neurons) and control SGNs (*c-Maf*$^{fl/fl}$, N=3 mice, n= 1669 neurons) and independently on SGNs from *Mafb*^{cKO} mice (*bhlhe22*$^{Cre/+}$*;Mafb*$^{fl/GFP}$, N=3, n= 1058 neurons) and their littermate controls (*Mafb*$^{fl/GFP}$, N=3 mice, n= 1172 neurons). Each comparison revealed control Ia, Ib, and Ic clusters and three knockout clusters corresponding to the three SGN subtypes, as identified by expression of known marker genes (**Figure 4B,C**). This result suggests that c-Maf and Mafb regulate gene expression in all three SGN subtypes, consistent with their pan-SGN expression. Comparison of all control and knockout SGNs, independent of subtype identity, revealed overlapping yet distinct sets of differentially expressed genes in c-Maf^{cKO} and Mafb^{cKO} SGNs (**Figure 4D**). Gene ontology analysis on overlapping genes revealed overrepresentation of molecules involved in synaptic composition and cell metabolism (**Figure 4E**); synaptic genes were also enriched in each individual mutant. In addition, we found that *Mafb* expression increased in *c-Maf* knockouts and *c-Maf* expression decreased in *Mafb* knockouts (**Figure 4F**). Therefore, it is difficult to extract the contribution of each individual factor by analyzing single mutant transcriptomes alone. These results suggest that c-Maf and Mafb participate in a feedback loop that influences how much of each factor is available and ultimately generates distinct programs of gene expression in SGNs.

To identify the combined effects of Maf factors on SGN gene expression, we collected SGN transcriptomes from cDKO (*bhlhe22*$^{Cre/+}$*;Mafb*$^{fl/fl}$*;c-Maf*$^{fl/fl}$, N=3 mice, n=705 SGNs) and control (*Mafb*$^{fl/fl}$*;c-Maf*$^{fl/fl}$, N=3 mice, n=907 SGNs) littermates. Unsupervised graph-based clustering revealed that control SGNs formed three distinct clusters that corresponded to Ia, Ib, and Ic SGN subtypes. By contrast, cDKO neurons formed one cluster that was well-separated from control neurons (**Figure 5A**). Comparison to controls suggested that the cDKO neurons acquire a hybrid Ib/Ic identity, since most of the cDKO cells expressed Ib and Ic genes such as *Runx1* and lacked expression of Ia genes such as *Rxrg*. However, cDKO neurons did not cluster with control Ib and Ic neurons and had lower expression of *Lypd1,* a Ic marker, compared to Ic neurons in controls. There were also a few *Lypd1*-negative neurons that were slightly segregated from the other cDKO SGNs, suggesting a low degree of molecular diversification (**Figure 5A**). Recent work has shown that Ia SGNs downregulate *Runx1* over development whereas the sustained expression of *Runx1* directs SGNs to a Ib/Ic subtype identity (Petitpré et al., 2022; Sanders and Kelley, 2022; Shrestha et al., 2023). Unlike c-Maf and Mafb single knockouts, cDKO SGNs did not segregate into three distinct subtypes. This means that Runx1, which continues to be expressed, cannot direct SGNs to mature Ib and Ic identities in the absence of c-Maf and Mafb. These results suggest that *c-Maf* and *Mafb* function together to promote SGN diversification and hence differentiation.

Comparison of control and cDKO SGNs identified 3024 significantly differentially expressed genes (DEG). Gene ontology analysis demonstrated that many of these genes were synaptic (**Figure 5B**). Notably, some cDKO DEG did not change in either of the single knockouts, confirming that c-Maf and Mafb may act interchangeably in some contexts (**Figure 5C, Figure S5**). Additionally, some genes were affected in different ways in c-Maf^{cKO}, Mafb^{cKO}, and cDKO SGNs (**Figure 5C**). Given their complementary patterns of expression, we reasoned that c-Maf and Mafb might have different effects on gene expression in each subtype. To

investigate this possibility, we focused on the top 50 upregulated genes and top 50 downregulated genes from the cDKO animals. Consistent with their Ib/Ic nature, many of the top upregulated genes are normally expressed at higher levels in Ib and Ic SGNs, whereas many of the downregulated genes tend to be enriched in Ia SGNs. 91/100 of these genes also changed expression in one or both of the single mutant datasets, but to different degrees in Ia, Ib, and Ic subtypes. For c-Maf^{cKO} SGNs, 45/75 genes (60%) demonstrated larger fold changes in Ia and Ib SGNs. On the other hand, Mafb^{cKO} SGNs tended to show larger fold changes in Ib and Ic SGNs (45/81 genes, 55.6%) (**Figure 5D,E**). Additionally, of the 63 genes that were differentially expressed in both single mutants, 20 actually changed in opposite directions. For instance, *Dcc*, which encodes the Netrin-1 receptor and is enriched in Ib/Ic SGNs, was upregulated in c-Maf^{cKO} SGNs and downregulated in Mafb^{cKO} neurons. Furthermore, in c-Maf^{cKO} SGNs, *Dcc* was most strongly upregulated in Ia SGNs whereas in Mafb^{cKO} SGNs, *Dcc* was most strongly downregulated in Ib and Ic SGNs (**Figure 5D,E**). Since *Mafb* is upregulated in c-Maf^{cKO} Ia SGNs (**Figure 4F**), this result suggests that *Dcc* is only expressed when the Mafb:c-Maf ratio is high. In accordance, *Dcc* is downregulated in cDKO SGNs. In other cases, the direction of the effect was the same, but one Maf factor appeared to play a dominant role. For example, *Calb2*, which encodes a calcium binding protein that is enriched in Ia SGNs, was strongly downregulated in c-Maf^{cKO} SGNs, barely affected in Mafb^{cKO} SGNs, and undetectable in cDKO SGNs (**Figure 5D-F**). Immunostaining confirmed decreased Calb2 in c-Maf^{cKO} animals, regardless of whether they also lacked one copy of *Mafb* or not (**Figure 5G** and **S5**). As predicted by scRNA-seq, the decrease in Calb2 was even stronger in the cDKO animals (**Figure 5G**). In this case, c-Maf appears to dominate, since the upregulation of Mafb was not sufficient to induce high levels of *Calb2* in c-Maf^{cKO} SGNs. Consistent with this interpretation, there was no obvious loss of Calb2 from Mafb^{cKO} SGNs, but there was an intermediate effect on Calb2 expression in Mafb^{cKO} SGNs that were also heterozygous for *c-Maf* (**Figure 5G** and **S5**). Thus, progressive loss of c-Maf causes graded expression of Calb2 that is fine-tuned by the presence of Mafb. Collectively, these results suggest that differences in the amount of c-Maf and Mafb help to establish subtype-specific patterns of gene expression.

Discussion

Functional diversity among neurons endows sensory systems with the capacity to encode complex sensory information. In the auditory system, spiral ganglion neurons (SGNs) exhibit functional, molecular, and synaptic differences that allow them to collectively capture the rich array of sounds encountered in the environment, even when there is background noise. Here, we show that two related transcription factors cooperate to generate synaptic and functional response properties across SGN subtypes. We find that c-Maf and Mafb establish both shared and subtype-specific features of SGN peripheral synapses that influence auditory responses. Likewise, c-Maf and Mafb regulate distinct programs of gene expression that include both shared and unique genes associated with the synapse and other aspects of mature neuronal function. In parallel, c-Maf and Mafb seem to work redundantly to control expression of genes needed for both subtype diversification and synaptic differentiation, as revealed by analysis of double mutant mice. Collectively, our data point to a model in which subtype-specific synaptic properties are shaped by the relative levels of c-Maf and Mafb, which vary across subtypes. We suggest that by executing both distinct and partially overlapping gene expression programs in

SGN subtypes, c-Maf and Mafb can combinatorially promote gene expression programs that establish and diversify SGN synaptic properties.

Our data support the idea that c-Maf and Mafb are part of a combinatorial transcriptional program that regulates gene expression in a subtype-specific manner. Histological protein and RNA measurements as well as single-cell RNA sequencing demonstrated that c-Maf and Mafb are expressed in complementary patterns across SGN subtypes, with c-Maf highest in Ia SGNs and Mafb highest in Ib/Ic SGNs. These data suggest that c-Maf has more influence over gene expression in Ia neurons, while Mafb has more influence over gene expression in Ib/Ic SGNs. Consistent with this idea, loss of either transcription factor had distinct effects on synapses, functional output and gene expression. Further, many of the Maf-dependent genes are normally expressed in a subtype-specific fashion, exemplified by Calb2 which is expressed at high levels in cells with high c-Maf levels. Moreover, upregulation of Mafb is not sufficient to restore Calb2 expression in the absence of c-Maf, further indicating that these two Maf factors are not functionally equivalent. Therefore, one possibility is that the respective levels of c-Maf and Mafb result in distinct transcriptional outcomes, due perhaps to differences in their binding affinity. Additionally, differences in their structure may alter how c-Maf and Mafb bind to loci in the genome. Finally, gene expression may be further shaped by which loci are accessible to either factor in each SGN subtype. More detailed analysis of chromatin structure and Maf factor binding affinities is needed to understand how a Maf code might work at the molecular level.

The effects of each Maf factor on gene expression may also be influenced by interactions with each other and other transcriptional regulators. c-Maf and Mafb can heterodimerize with each other and homodimerize with themselves (Pogenberg et al., 2014; Rodríguez-Martínez et al., 2017; Suda et al., 2014; Yang and Cvekl, 2016). This ability for homo- and heterodimerization provides a basis for combinatorial and synergistic control of gene expression (Rodríguez-Martínez et al., 2017). It has been shown that mutations that force Mafb to only form homodimers result in binding of symmetrical Maf recognition element (MARE) DNA binding sites. Meanwhile, mutant forms of Mafb that could only form heterodimers with the immediate early gene (IEG) cFos had entirely different DNA binding preferences (Pogenberg et al., 2014). The extent of hetero- and homodimerization among c-Maf, Mafb, and cFos could depend on the relative levels and binding preferences of available dimerization partners. Our discovery that c-Maf and Mafb stoichiometry varies across SGN subtypes suggests one potential mechanism for nuanced differences in the control of gene expression. Further work assessing protein-protein interactions in SGNs is needed to determine which dimers are present, as well as their effects on gene expression.

Although synaptic punctum size and position correlates strongly with SGN subtype identity, there is also synaptic heterogeneity within subtypes that cannot be explained by Maf expression. The potential for interactions with IEGs such as cFos raises the possibility that c-Maf and Mafb act as conduits between incoming activity and synaptic refinement. Indeed, previous work has established an important role for neuronal activity in diversifying SGN subtypes consistent with the effects of spontaneous and experience-dependent activity on cochlear circuit assembly (Shrestha et al., 2018; Sun et al., 2018). Neuronal activity stimulates the expression of IEGs such as cFos and cJun, which induce transcription of a cohort of genes that encode proteins that are localized to or act at synapses (Joo et al., 2016; Sheng and Greenberg, 1990). Both c-Maf and Mafb can dimerize with cFos, while only Mafb can dimerize

with cJun, offering additional opportunity for activity-dependent effects within subtypes (Yang and Cvekl, 2016). Relevant activity could come either from the IHCs, which have highly heterogeneous presynaptic release sites (Meyer et al., 2009; Özçete and Moser, 2021; Payne et al., 2021), or from the olivocochlear efferents, which form more synapses on Ib and Ic SGNs than on Ia SGNs (Hua et al., 2021). Indeed, severing of olivocochlear efferents in adult mice is sufficient to alter synapse punctum size (Yin et al., 2014). Both c-Maf and Mafb are expressed in adults and could contribute to this kind of plasticity, as well as the maintenance of subtype-specific synaptic properties throughout life.

In addition to their relatively subtle effects on subtype-related synaptic properties, Maf factors act synergistically to diversify SGN subtypes and promote synaptic differentiation more generally. Although Ia, Ib, and Ic SGNs could be identified in each single mutant, the double mutant SGNs formed a single cluster that expressed Ib and Ic marker genes but not Ia marker genes. This phenotype is fundamentally different from what occurs in *Runx1* conditional knock-out mice, where many mutant Ib and Ic SGNs take on Ia SGN molecular identities that co-cluster with control Ia SGNs (Shrestha et al., 2023). Without any Maf factors, SGNs are unable to split into three distinct identities. Thus, our work suggests that Maf factors help to execute subtype specification programs initiated by Runx1 and/or other undefined transcription factors. This phenotype fits with recent observations that developing SGNs pass through a shared Ib/Ic precursor state characterized by expression of *c-Maf* and *Mafb* (Sanders and Kelley, 2022). Although cDKO SGNs appear to retain some aspects of this hybrid identity, development is not arrested in the cDKO SGNs, which still send peripheral processes towards hair cells and make post-synaptic densities that appose pre-synaptic ribbons, albeit in an aberrant manner. Thus, other as yet unidentified factors likely regulate additional gene expression programs necessary for these wiring events. Additionally, while we have focused on synaptic phenotypes, c-Maf and Mafb may also influence other subtype-specific properties, such as excitability. Indeed, genes that encode channels also depend on Maf activity, though additional work is needed to determine which genes are direct targets and which might change as a result of altered synaptic signaling. Altogether, the development of functional synapses with subtype-specific features seems to rely on the combined activity of Maf factors that work together to induce a general synaptic differentiation program and separately to shape that program according to cell identity.

The formation of functionally and morphologically heterogeneous synapses is essential for proper circuit function. Our results show one mechanism by which synapse identity can be linked to neuronal identity. In more complex circuits, individual neurons can make many different types of synapses, making it challenging to identify relevant proteins or to understand how subtle differences in protein composition impact synaptic function. In SGNs, synaptic heterogeneity can be studied at the level of the neuron. To our knowledge, this is the first description of a combinatorial code for synaptic differentiation. A deeper understanding of how c-Maf and Mafb and their target genes build synapses with different properties in SGNs will inform how synapse heterogeneity arises in other neuron types.

Acknowledgements: Thank you to Dr. Winthrop Gillis for assistance with code, Dr. Bernardo Sabatini for access to the 10x Chromium controller, the Bauer Core Facility (Harvard University) for sequencing our samples, and to Dr. Brikha Shrestha for helpful feedback on the manuscript.

This work was supported by DC R010009223 (to LVG), DCF32DC019009 (to AAS), and an HHMI Gilliam Fellowship (to IMB).

Author contributions: IMB conceived of the project, performed experiments, analyzed results, and wrote the manuscript. LL, CMR, and AAS performed experiments and analyzed results. AY and WY initially discovered the *c-Maf* and *c-Maf;Mafb* double mutant phenotypes. LVG conceived of the project, interpreted results, and wrote the manuscript.

METHODS:

Animal Models:

Bhlhe22$^{Cre/+}$ (*Bhlhe22*$^{Cre/+}$, MGI:4440745), *c-Maf*^{fl} (MGI:5316775), *Mafb*^{fl} (MGI:5581666) and Rosa26-LSL-tdTomato (*Ai14*; Jax strain 007914) are all previously described. *NetrinG1*$^{Cre/+}$ mice were kindly provided by Fan Wang (Bolding et al., 2020). Animals were maintained on a mixed background. Animal work was conducted in compliance with protocols approved by the Institutional Animal Care and Use Committee at Harvard Medical School.

Immunostaining

Animals were anesthetized via isoflurane exposure in an open-drop chamber and subsequently perfused with cold 4% paraformaldehyde (PFA) in 1X PBS. Both temporal bones were dissected and cold 4% PFA was perfused through the oval window with a syringe. For wholemount immunohistochemistry, cochleae were drop-fixed in 4% PFA at room temperature and transferred to 10% EDTA overnight at 4C. Cochlea were then micro-dissected and transferred to blocking solution (16%v/v normal donkey serum, 3%v/v Triton-X in 1xPBS) overnight at 4ºC. Cochlear turns were stained overnight with anti-Calb2 (1:1000, Swant CG1), anti-CTBP2 (1:500, BD Transduction Laboratories, Clone 16) and anti-GluA2 (1:500, EMB Millipore MAB 397) and subsequently with corresponding secondaries at 37ºC overnight. Rinses after primary and secondary antibody incubation were done using 1% PBST for 10 minutes at room temperature. Cochleae used for cryosectioning and staining were drop-fixed overnight at 4ºC in 4% PFA in 1x PBS and then transferred to 120mM EDTA for three nights. Cochleae were then immersed in a sucrose gradient from 10% to 30% at 4°C prior to embedding. 18 µm cochlear sections were washed 1x for 5 minutes in 1x PBS and then 2x for 5 minutes in 0.25% Triton X-100 in 1x PBS. Sections were blocked with 5%v/v normal donkey serum and 0.3% Triton X-100 in 1x PBS. Sections were stained with a compatible combination of: rabbit anti-MAFB (1:250, Novus Biologicals, NBP1-81342), rabbit anti c-Maf (1:250, Bethyl Labs A700-045), goat anti CALB2 (1:500, Swant CG1) for four hours at room temperature. After rinsing with 1x PBS, sections stained with appropriate secondary antibodies at 4ºC overnight. Sections were then rinsed with 1x PBS for 10 minutes. The second wash contained DAPI at 1 mg/uL.

Image acquisition

All tissues were imaged using a Leica SP8 point-scanning confocal microscope with HyD and photomultiplier tube (PMT) detectors. For wholemount cochleae, frequency maps were generated by taking 10X stacks of the cochlear turns and using the Measure_Line ImageJ plugin available through the Histology Core at Mass Eye and Ear (Boston, MA). Synaptic puncta were then captured using HyD detectors while hair cells were captured using PMT detectors using a 63x oil-immersion objective (voxel size= 0.901 x 0.901 x 0.299um^3). Special

attention was taken not to oversaturate any pixels in channels that were to be used for intensity-based morphometric quantification.

Image analysis

Pre- and post-synaptic puncta were reconstructed semi-automatically using the “Surfaces” function in Imaris. A local contrast-background subtraction algorithm was applied to all z-stacks for thresholding. All reconstructions were created and reviewed with the researcher blinded to genotype. Inaccuracies in automatic segmentation were corrected manually. Reconstructions located outside the volume of hair cells were excluded from analysis. Image-based coordinates of reconstructed puncta were transformed into hair cell-centric coordinates using the “Reference Frames” function in Imaris. Each hair cell-centric coordinate system was defined with the following three planes: an XZ plane bisecting the hair cell through its plane of symmetry, a YZ plane bisecting the nucleus through the plane parallel to the tilt of the hair cell, and an XY plane tangential to the basolateral pole of the hair cell. Metrics regarding the size and localization of reconstructed pre- and postsynaptic puncta were exported into Excel for further analysis. For quantification of c-MAF and MAFB stains, 3D reconstructions were made for each SGN cell body in Imaris similar as above using the HuD channel that marked all SGN cell bodies. Metrics regarding fluorescence intensity were exported into excel for further analysis.

Auditory response testing

Mice were anesthetized with an intraperitoneal injection of ketamine (100 mg/kg) and xylaxine (10 mg/kg). Meloxicam (1 mg/kg) was administered intraperitoneally for analgesia. Animals were placed on a 37ºC heating pad (ATC1000, World Precision Instruments) and additional ketamine (30-40 mg/kg) was administered as needed to maintain the anesthetic plane throughout the procedure. ABRs and DPOAEs were measured using a custom acoustic system (Eaton-Peabody Laboratories, Massachusetts Eye and Ear) in an electrically shielded and sound attenuating chamber. All recordings were performed with the researcher blinded to genotype.

Auditory brainstem responses (ABRs) were recorded from three subcutaneous needle electrodes: a recording electrode caudal to the pinna, a reference electrode at the vertex, and a ground electrode by the tail. ABR stimuli were presented from 20 to 90 dB SPL in 5 dB steps at 8, 16, 32, and 45 kHz. Each stimulus was presented as a 5-ms tone-pip at a rate of 31/s, with a 0.5 ms rise-fall time and alternating polarities. Responses were amplified 10,000x, filtered with a 0.3–3 kHz passband (P511, Grass), and averaged 512 times. Recordings with peak to peak amplitudes exceeding 15 μV were rejected as artifacts. ABR thresholds, amplitudes, and latencies were analyzed using ABR Peak Analysis software (v.1.1.1.9; Massachusetts Eye and Ear). ABR threshold was defined as the lowest stimulus level at which wave 1 could be identified by visual inspection.

Distortion product otoacoustic emissions (DPOAEs) were recorded from a probe-tube microphone aligned above the ear canal. In-ear calibrations were performed using the Cochlear Function Test Suite (v 2.36, Massachusetts Eye and Ear) prior to reach recording. DPOAE stimuli were presented at primary tones f1 and f2, where f2 varied from 5.6 to 32 kHz in half-

octave steps. Primary tones were presented at frequency ratios of f2/f1 = 1.2 and level differences of L1 = L2 + 10. Levels of primary tone f2 were incremented in 10 dB steps from 0 to 70 dB SPL. The distortion products at 2f1-f2 were temporally and spectrally averaged. Iso-response contours were generated by the Cochlear Function Test Suite software for various criterion response amplitudes. DPOAE threshold was defined as the f1 level required to produce a DPOAE of 5 dB SPL.

Single-cell RNA sequencing

Library Preparation
Temporal bones were extracted, and the spiral ganglion was microdissected from the cochlea in cold Leibovitz L-15 buffer. Cells were then treated with collagenase type IV followed by papain for 25 minutes each at 37°C. The cells were passed through ovomucoid as recommended for the Papain Dissociation System and then passed through a 40 µm cell strainer. Dissociated cells were resuspended in cold EBSS. Cell concentration was estimated using a hemocytometer. Cells were then loaded into a single cell chip from 10x Genomics following manufacturer's recommendations. Datasets were processed with the Chromium single-cell 3' library and gel bead kit v2.0. cDNA libraries were generated according to the manufacturer's directions. The final libraries were sequenced on an Illumina NovaSeq SP.

Bioinformatics Analysis:

Alignment
Raw reads were converted to fastq files using the cellranger pipeline from 10X Genomics v 3.0.1. Reads were then aligned to the mouse reference genome (mm10) in a Linux-based high performance computing cluster at Harvard Medical School.

Normalization
The aligned data was imported into R and analyzed for statistical analysis and graphical representation. The library was normalized by fitting the gene counts to a regularized binomial regression function implemented by the scTransform package for Seurat using all default settings and regression on percent mitochondrial reads.

Clustering and Subclustering
Clustering was performed using the Seurat FindClusters command using 30 principle components. SGN clusters were identified and subsetted out by the expression of neuronal genes such as Tubb3 and Nefh. Utilizing the RNA assay, subsetted SGNs were normalized and subclustered using similar parameters as above. Subtypes of SGNs were identified by the expression of subtype specific markers previously identified (Calb2, Lypd1, and Runx1). Differential expression was tested using the FindAllMarkers command on the SCT assay.

Differential Gene Expression and Gene Ontology Analysis
Differential expression was tested using the FindAllMarkers command on the SCT assay and probing for significantly regulated genes between control and mutant SGNs from each genotype. The differential expression of cDKO genes was analyzed by subtype in each single

cKO dataset. Genes were considered differentially expressed in mutant SGNs if they were significantly changed (P<0.05) at a Log2Fold change greater than 0.25. Differentially expressed genes were subjected to Gene Ontology term enrichment analysis in DAVID.

Statistics

All statistical analysis was done in Python. Normality of each distribution was tested using the Shapiro-Wilk test. If both groups showed a normal distribution, a parametric t-Test or ANOVA was used. Otherwise, the non-parametric Mann-Whitney Rank Sum or Kruskal-Wallis Test was applied. Statistical analysis for differentially expressed genes was done in R. Differential gene expression was tested using a Wilcoxon rank sum test with Bonferroni post-hoc correction. Gene ontology categories with a bonferroni-adjusted P<0.001 were considered significant.

Figure Legends

Figure 1. c-Maf and Mafb have opposing and additive effects on SGN synapses. (A) Wholemount immunostaining for the synaptic proteins GluA2 and CTBP2 in the 16 kHz region of cochleae from control (NoCre, *Mafb*$^{fl/fl}$*;c-Maf*$^{fl/fl}$, N=15, orange), *c-Maf* knockout (*c-Maf*^{cKO}, *bhlhe22*$^{Cre/+}$*;Mafb*$^{fl/+}$*;c-Maf*$^{fl/fl}$, N=9, green), *Mafb* knockout (*Mafb*^{cKO}, *bhlhe22*$^{Cre/+}$*;Mafb*$^{fl/fl}$*;c-Maf*$^{fl/+}$, N=7, magenta), and double knockout (cDKO, *bhlhe22*$^{Cre/+}$*;Mafb*$^{fl/fl}$*;c-Maf*$^{fl/fl}$, N=10, blue), littermates. Hair cells were stained for Calb2 (not shown) and are outlined in dashed lines in the merge panels. Volume measurements were normalized by the median of the control values within each stain batch. Scale bar, 5µm. Yellow arrowheads indicate small puncta in cDKO animals. **(B)** Distribution of GluA2 puncta volumes in control (NoCre), *Mafb*^{cKO,} *c-Maf*^{CKO} and cDKO animals (Kruskal-Wallis, p<0.001). **(C)** Median GluA2 puncta volumes per animal across genotypes (Kruskal-Wallis, p=0.030). **(D)** Mean interquartile range of GluA2 puncta volumes per mouse across genotypes (Kruskal-Wallis, p<0.001). **(E)** Mean GluA2 inter-punctum distance per animal across genotypes (Kruskal-Wallis, p<0.001).

Figure S1. Cochlear phenotypes in Maf mutants. (A) Wholemount immunostaining of neurofilament in cochleae from control animals (NoCre, *Mafb*$^{fl/fl}$*;c-Maf*$^{fl/fl}$, N=6), *c-Maf* knockout (*c-Maf*^{cKO}, *bhlhe22*$^{Cre/+}$*;Mafb*$^{fl/+}$*;c-Maf*$^{fl/fl}$, N=1), *Mafb* knockout (*Mafb*^{cKO}, *bhlhe22*$^{Cre/+}$*;Mafb*$^{fl/fl}$*;c-Maf*$^{fl/+}$, N=1), and double knockout (cDKO, *bhlhe22*$^{Cre/+}$*;Mafb*$^{fl/fl}$*;c-Maf*$^{fl/fl}$, N=7) littermates. Scale bar, 100µm. **(B)** scRNAseq expression levels of *c-Maf* in lateral olivocochlear effects (LOC), medial olivocochlear efferents (MOC) and faciobrachial motor neurons. **(C)** scRNAseq expression levels of *Mafb* in lateral olivocochlear effects (LOC), medial olivocochlear efferents (MOC) and faciobrachial motor neurons (Frank et al., 2023) **(D-F)** Unnormalized data from Figure 1B-D. **(G-H)** GluA2 puncta volumes in control (NoCre, *c-Maf*$^{fl/fl}$) and *c-Maf*^{CKO} (*bhlhe22*$^{Cre/+}$*;c-Maf*$^{fl/fl}$) animals (t-test, p<0.001).

Figure 2. *c-Maf* and *Mafb* have opposing and additive effects on auditory function. Auditory brainstem responses (ABRs) were recorded from 8-12 week old control animals (NoCre, *Mafb*$^{fl/fl}$*;c-Maf*$^{fl/fl}$, N=14, orange), *c-Maf* knockout (c-Maf^{cKO}, *bhlhe22*$^{Cre/+}$*;Mafb*$^{fl/+}$*;c-Maf*$^{fl/fl}$, N=6, green), *Mafb* knockout (Mafb^{cKO}, *bhlhe22*$^{Cre/+}$*;Mafb*$^{fl/fl}$*;c-Maf*$^{fl/+}$, N=11, magenta), and double knockout (cDKO, *bhlhe22*$^{Cre/+}$*;Mafb*$^{fl/fl}$*;c-Maf*$^{fl/fl}$, N=9, blue) littermates. **(A-D)** Average ABR waveforms recorded after presentation of a 16kHz stimulus at different sound intensity levels across genotypes. Standard error shown by shaded bands. **(E)** ABR threshold measurements

across frequencies (Kruskal-Wallis, $p_{8kHz}<0.001$, $p_{16kHz}<0.001$, $p_{32kHz}=0.157$, $p_{45kHz}=0.293$). **(F)** Overlaid average ABR waveforms of Peak 1 (P1) across genotypes in response to a 16kHz, 80 dB SPL (decibel sound pressure level) sound stimulus in control animals (NoCre, orange), *c-Maf* knockout (c-Maf^{cKO}, green), *Mafb* knockout (Mafb^{cKO}, magenta), and double knockout (cDKO, blue) littermates. **(G)** P1 amplitude across all sound intensities for a 16 kHz stimulus. Comparisons with an asterisk were statistically significant (p<0.05, Kruskal-Wallis). Significant differences amongst groups that had a Kruskal-Wallis p- value<0.05 were followed with a pairwise post-hoc Dunn test. Kruskal-Wallis p-values and pairwise post-hoc Dunn p-values can be found in Supplemental Table 2.

Figure S2. Outer hair cell function and Peak I latency in Maf mutants. (A) DPOAE thresholds across all frequencies. Standard error shown by vertical bars (all comparisons not significant, p>0.05, Kruskal-Wallis). **(B)** P1 latency across sound pressure levels for a 16 kHz stimulus. Comparisons with an asterisk were statistically significant (p<0.05, Kruskal-Wallis). Significant differences amongst groups that had a Kruskal-Wallis p-value<0.05 were followed with a pairwise post-hoc Dunn test. Kruskal-Wallis p-values and pairwise post-hoc Dunn p-values can be found in Supplemental Table 2.

Figure 3. Complementary expression of c-Maf and Mafb across SGNs. (A) scRNAseq expression profiles of *c-Maf* and a Ia-enriched gene, *Rxrg* (Shrestha et al., 2018). **(B)** scRNAseq profiles of *Mafb* and a Ib/Ic-enriched gene *Ntng1* (Shrestha et al., 2018)**. (C)** Immunolabeling of c-Maf and Calb2 in cochlear sections of P28-P30 wildtype mice (N=3). Calb2 is differentially expressed in SGN subtypes at this stage (highest in Ia SGNs, lowest in Ic SGNs) **(D)** Positive correlation between standardized (z-scored) staining intensities for c-Maf and Calb2 ($R^2=0.55$, p<0.001). **(E)** Fluorescent tdTomato labeling of *Ntng1$^{Cre/+}$;Ai14/+* cells (magenta) with immunolabeling for c-Maf (cyan) in sections through the cochlea of P6 mice (N=4). Example tdTomato+ (red arrowheads) and tdTomato- (white arrowheads) SGNs are indicated. Glia (yellow arrowheads) were excluded by the intensity of tdTomato, smaller cell body size, fried-egg like morphology and lack of Calb2 expression, yellow arrowheads. tdTomato+ SGNs will develop as Ib or Ic SGNs, whereas tdTomato- could develop as any of the three subtypes. **(F)** Quantification of standardized c-Maf staining intensity in *Ntng1$^{Cre/+}$;Ai14/+* labeled and unlabeled P6 SGNs. Each dot corresponds to a single reconstructed cell (p=<0.001, Mann-Whitney Rank sum with Bonferroni correction). **(G)** Immunostaining for Mafb (cyan) and tdTomato (magenta) in sections through the cochlea of P6 *Ntng1$^{Cre/+}$;Ai14/+* mice (N=4), with example tdTomato+ (red arrowheads) and tdTomato- (white arrowheads) SGNs indicated and shown at higher power in **G'**. **(H)** Quantification of standardized Mafb staining intensity in *Ntng1$^{Cre/+}$;Ai14/+* labeled and unlabeled P6 SGNs. Each dot corresponds to a single reconstructed cell. (p=<0.001, Mann-Whitney Rank sum with Bonferroni correction).

Figure 4. c-Maf and Mafb maintain subtype differentiation and regulate overlapping yet distinct sets of synaptic genes. (A) Dotplot summarizing relative *c-Maf* and *Mafb* expression across SGN subtypes. Red denotes higher relative expression and cyan denotes lower relative expression. **(B)** UMAP plot summarizing sequencing data of 1669 control SGNs (*bhlhe22$^{Cre/+}$; c-Maf$^{fl/+}$,* N=6) and 1708 c-Maf^{cKO} SGNs (*bhlhe22$^{Cre/+}$; c-Maf$^{fl/fl}$,* N=3). **(C)** UMAP plot summarizing sequencing data of 1172 control SGNs (*Mafb$^{fl/+}$,* N=3) and 1058 Mafb^{cKO} SGNs (*bhlhe22$^{Cre/+}$;*

Mafb$^{fl/GFP}$, N=4). **(D)** Relative distribution of genes that are differentially expressed in either or both Mafb^{cKO} and c-Maf^{cKO} animals. **(E)** Cellular component gene ontology analysis of genes upregulated in both Mafb^{cKO} and c-Maf^{cKO} animals. Gray line denotes Bonferroni- adjusted p=0.001 **(F)** Expression of *c-Maf* and *Mafb* in Mafb^{cKO} and c-Maf^{cKO} animals compared to controls.

Figure S4. Gene Ontology on c-Maf^{cKO} and Mafb^{cKO} differentially expressed genes. Gene ontology analysis of differentially expressed genes (DEG) in Mafb **(A)** and c-Maf **(B)** mutant animals. Gene ontology was performed separately on upregulated and downregulated genes. Gray line denotes Bonferroni-adjusted p=0.001.

Figure 5. Synergistic and subtype-specific effects on gene expression in c-Maf/Mafb^{cDKO} SGNs. (A) UMAP plot summarizing sequencing data of double knockout (cDKO, *bhlhe22*$^{Cre/+}$*;Mafb*$^{fl/fl}$*;c-Maf*$^{fl/fl}$, N=3, n=763) SGNs and controls (*Mafb*$^{fl/fl}$*;c-Maf*$^{fl/fl}$, N=3, n=974). Inset plots display expression of the Ia marker *Rxrg*, the Ib/Ic marker *Runx1*, and the Ic marker *Lypd1* in control and cDKO SGNs. **(B)** Cellular component gene ontology analysis of differentially expressed genes (DEG) in cDKO animals. Gene ontology was performed separately on upregulated and downregulated genes. Gray line denotes Bonferroni-adjusted p=0.001 **(C)** Dot plot of top 100 differentially expressed genes in cDKO mutant SGNs. The size of the dot represents the percent of cells that had an expression level above 0. Genes are organized by whether they were changed in both single mutant in the same or opposite directions, or changed in only one single mutant or only changed in the double mutants. **(D)** Log fold changes in gene expression of the top 100 cDKO DEGs in c-Maf^{cKO} SGNs. **(E)** Log fold changes in gene expression of top 100 cDKO DEGs in Mafb^{cKO} SGNs. Purple dots denote genes that were changed in the same direction in each single CKO dataset. Green dots denote genes that were changed in opposite directions. Magenta dots highlight how the Maf factors changed expression in each single cKO. **(F)** *Calb2* expression levels in c-Maf^{cKO}, Mafb^{cKO} and cDKO SGNs. **(G)** Immunohistochemical stains of Calb2 in sections through the cochlea of adult single and cDKO mutants. Scale bar= 20µm.

Figure S5. Gene Ontology Analysis. (A) Gene ontology analysis of differentially expressed genes (DEG) in cDKO animals. Gene ontology was performed separately on upregulated and downregulated genes. **(B)** Molecular function gene ontology analysis of differentially expressed genes (DEG) in cDKO animals. Gray line denotes Bonferroni-adjusted p=0.001. **(C)** Immunohistochemical stains of Calb2 in sections through the cochlea of adult c-Maf^{cKO} (*bhlhe22*$^{cre/+}$*;cMaf*$^{fl/fl}$) and control littermate (*cMaf*$^{fl/fl}$). **(D)** Immunohistochemical stains of Calb2 in sections through the cochlea of adult Mafb^{cKO} (*bhlhe22*$^{cre/+}$*;Mafb*$^{fl/GFP}$) and control littermate (*Mafb*$^{fl/+}$). Scale bars= 20µm.

References

Appler, J.M., Lu, C.C., Druckenbrod, N.R., Yu, W.-M., Koundakjian, E.J., Goodrich, L.V., 2013. Gata3 Is a Critical Regulator of Cochlear Wiring. Journal of Neuroscience 33, 3679–3691. https://doi.org/10.1523/JNEUROSCI.4703-12.2013

Bolding, K.A., Nagappan, S., Han, B.-X., Wang, F., Franks, K.M., 2020. Recurrent circuitry is required to stabilize piriform cortex odor representations across brain states. eLife 9, e53125. https://doi.org/10.7554/eLife.53125

Coate, T.M., Scott, M.K., Gurjar, M., 2019. Current concepts in cochlear ribbon synapse formation. Synapse 73, e22087. https://doi.org/10.1002/syn.22087

Druckenbrod, N.R., Goodrich, L.V., 2015. Sequential Retraction Segregates SGN Processes during Target Selection in the Cochlea. J. Neurosci. 35, 16221–16235. https://doi.org/10.1523/JNEUROSCI.2236-15.2015

Frank, M.M., Sitko, A.A., Suthakar, K., Torres Cadenas, L., Hunt, M., Yuk, M.C., Weisz, C.J., Goodrich, L.V., 2023. Experience-dependent flexibility in a molecularly diverse central-to-peripheral auditory feedback system. eLife 12, e83855. https://doi.org/10.7554/eLife.83855

Goodrich, L.V., 2016. Early Development of the Spiral Ganglion, in: Dabdoub, A., Fritzsch, B., Popper, A.N., Fay, R.R. (Eds.), The Primary Auditory Neurons of the Mammalian Cochlea, Springer Handbook of Auditory Research. Springer New York, New York, NY, pp. 11–48. https://doi.org/10.1007/978-1-4939-3031-9_2

Hu, N., Rutherford, M.A., Green, S.H., 2020. Protection of cochlear synapses from noise-induced excitotoxic trauma by blockade of Ca^{2+} -permeable AMPA receptors. Proc. Natl. Acad. Sci. U.S.A. 117, 3828–3838. https://doi.org/10.1073/pnas.1914247117

Hua, Y., Ding, X., Wang, H., Wang, F., Lu, Y., Neef, J., Gao, Y., Moser, T., Wu, H., 2021. Electron Microscopic Reconstruction of Neural Circuitry in the Cochlea. Cell Reports 34, 108551. https://doi.org/10.1016/j.celrep.2020.108551

Huang, L.-C., Barclay, M., Lee, K., Peter, S., Housley, G.D., Thorne, P.R., Montgomery, J.M., 2012. Synaptic profiles during neurite extension, refinement and retraction in the developing cochlea. Neural Dev 7, 38. https://doi.org/10.1186/1749-8104-7-38

Joo, J.-Y., Schaukowitch, K., Farbiak, L., Kilaru, G., Kim, T.-K., 2016. Stimulus-specific combinatorial functionality of neuronal c-fos enhancers. Nat Neurosci 19, 75–83. https://doi.org/10.1038/nn.4170

Kane, K.L., Longo-Guess, C.M., Gagnon, L.H., Ding, D., Salvi, R.J., Johnson, K.R., 2012. Genetic background effects on age-related hearing loss associated with Cdh23 variants in mice. Hearing Research 283, 80–88. https://doi.org/10.1016/j.heares.2011.11.007

Kiang, N., 1965. Discharge Patterns of Single Fibres in the Cat's Auditory Nerve, Massachusetts Institute of Technology. Research Laboratory of Electronics. Special technical report no. 13. Cambridge, Mass., M.I.T. Press.

Liberman, L.D., Liberman, M.C., 2016. Postnatal maturation of auditory-nerve heterogeneity, as seen in spatial gradients of synapse morphology in the inner hair cell area. Hearing Research 339, 12–22. https://doi.org/10.1016/j.heares.2016.06.002

Liberman, L.D., Wang, H., Liberman, M.C., 2011. Opposing Gradients of Ribbon Size and AMPA Receptor Expression Underlie Sensitivity Differences among Cochlear-Nerve/Hair-Cell Synapses. Journal of Neuroscience 31, 801–808. https://doi.org/10.1523/JNEUROSCI.3389-10.2011

Liberman, M.C., 1982. Single-Neuron Labeling in the Cat Auditory Nerve. Science 216, 1239–1241. https://doi.org/10.1126/science.7079757

Melcher, J.R., Kiang, N.Y.S., 1996. Generators of the brainstem auditory evoked potential in cat III: identified cell populations. Hearing Research 93, 52–71. https://doi.org/10.1016/0378-5955(95)00200-6

Meyer, A.C., Frank, T., Khimich, D., Hoch, G., Riedel, D., Chapochnikov, N.M., Yarin, Y.M., Harke, B., Hell, S.W., Egner, A., Moser, T., 2009. Tuning of synapse number, structure and function in the cochlea. Nat Neurosci 12, 444–453. https://doi.org/10.1038/nn.2293

Michanski, S., Smaluch, K., Steyer, A.M., Chakrabarti, R., Setz, C., Oestreicher, D., Fischer, C., Möbius, W., Moser, T., Vogl, C., Wichmann, C., 2019. Mapping developmental

maturation of inner hair cell ribbon synapses in the apical mouse cochlea. Proc. Natl. Acad. Sci. U.S.A. 116, 6415–6424. https://doi.org/10.1073/pnas.1812029116
Özçete, Ö.D., Moser, T., 2021. A sensory cell diversifies its output by varying Ca^{2+} influx-release coupling among active zones. The EMBO Journal 40. https://doi.org/10.15252/embj.2020106010
Pai, E.L.-L., Vogt, D., Clemente-Perez, A., McKinsey, G.L., Cho, F.S., Hu, J.S., Wimer, M., Paul, A., Fazel Darbandi, S., Pla, R., Nowakowski, T.J., Goodrich, L.V., Paz, J.T., Rubenstein, J.L.R., 2019. Mafb and c-Maf Have Prenatal Compensatory and Postnatal Antagonistic Roles in Cortical Interneuron Fate and Function. Cell Reports 26, 1157-1173.e5. https://doi.org/10.1016/j.celrep.2019.01.031
Payne, S.A., Joens, M.S., Chung, H., Skigen, N., Frank, A., Gattani, S., Vaughn, K., Schwed, A., Nester, M., Bhattacharyya, A., Iyer, G., Davis, B., Carlquist, J., Patel, H., Fitzpatrick, J.A.J., Rutherford, M.A., 2021. Maturation of Heterogeneity in Afferent Synapse Ultrastructure in the Mouse Cochlea. Front. Synaptic Neurosci. 13, 678575. https://doi.org/10.3389/fnsyn.2021.678575
Perkins, R.E., Morest, D.K., 1975. A study of cochlear innervation patterns in cats and rats with the Golgi method and Nomarski optics. J. Comp. Neurol. 163, 129–158. https://doi.org/10.1002/cne.901630202
Petitpré, C., Faure, L., Uhl, P., Fontanet, P., Filova, I., Pavlinkova, G., Adameyko, I., Hadjab, S., Lallemend, F., 2022. Single-cell RNA-sequencing analysis of the developing mouse inner ear identifies molecular logic of auditory neuron diversification. Nat Commun 13, 3878. https://doi.org/10.1038/s41467-022-31580-1
Petitpré, C., Wu, H., Sharma, A., Tokarska, A., Fontanet, P., Wang, Y., Helmbacher, F., Yackle, K., Silberberg, G., Hadjab, S., Lallemend, F., 2018. Neuronal heterogeneity and stereotyped connectivity in the auditory afferent system. Nat Commun 9, 3691. https://doi.org/10.1038/s41467-018-06033-3
Pogenberg, V., Consani Textor, L., Vanhille, L., Holton, S.J., Sieweke, M.H., Wilmanns, M., 2014. Design of a bZip Transcription Factor with Homo/Heterodimer-Induced DNA-Binding Preference. Structure 22, 466–477. https://doi.org/10.1016/j.str.2013.12.017
Rodríguez-Martínez, J.A., Reinke, A.W., Bhimsaria, D., Keating, A.E., Ansari, A.Z., 2017. Combinatorial bZIP dimers display complex DNA-binding specificity landscapes. eLife 6, e19272. https://doi.org/10.7554/eLife.19272
Ross, S.E., Mardinly, A.R., McCord, A.E., Zurawski, J., Cohen, S., Jung, C., Hu, L., Mok, S.I., Shah, A., Savner, E.M., Tolias, C., Corfas, R., Chen, S., Inquimbert, P., Xu, Y., McInnes, R.R., Rice, F.L., Corfas, G., Ma, Q., Woolf, C.J., Greenberg, M.E., 2010. Loss of inhibitory interneurons in the dorsal spinal cord and elevated itch in Bhlhb5 mutant mice. Neuron 65, 886–898. https://doi.org/10.1016/j.neuron.2010.02.025
Ryugo, D.K., 1992. The Auditory Nerve: Peripheral Innervation, Cell Body Morphology, and Central Projections, in: Webster, D.B., Popper, A.N., Fay, R.R. (Eds.), The Mammalian Auditory Pathway: Neuroanatomy, Springer Handbook of Auditory Research. Springer New York, New York, NY, pp. 23–65. https://doi.org/10.1007/978-1-4612-4416-5_2
Sanders, T.R., Kelley, M.W., 2022. Specification of neuronal subtypes in the spiral ganglion begins prior to birth in the mouse. Proc Natl Acad Sci U S A 119, e2203935119. https://doi.org/10.1073/pnas.2203935119
Sendin, G., Bulankina, A.V., Riedel, D., Moser, T., 2007. Maturation of Ribbon Synapses in Hair Cells Is Driven by Thyroid Hormone. Journal of Neuroscience 27, 3163–3173. https://doi.org/10.1523/JNEUROSCI.3974-06.2007
Sheng, M., Greenberg, M.E., 1990. The regulation and function of c-fos and other immediate early genes in the nervous system. Neuron 4, 477–485. https://doi.org/10.1016/0896-6273(90)90106-P

Shrestha, B.R., Chia, C., Wu, L., Kujawa, S.G., Liberman, M.C., Goodrich, L.V., 2018. Sensory Neuron Diversity in the Inner Ear Is Shaped by Activity. Cell 174, 1229-1246.e17. https://doi.org/10.1016/j.cell.2018.07.007

Shrestha, B.R., Goodrich, L.V., 2019. Wiring the Cochlea for Sound Perception, in: Kandler, K. (Ed.), The Oxford Handbook of the Auditory Brainstem. Oxford University Press, pp. xxx–36. https://doi.org/10.1093/oxfordhb/9780190849061.013.1

Shrestha, B.R., Wu, L., Goodrich, L.V., 2023. Runx1 controls auditory sensory neuron diversity in mice. Developmental Cell 58, 306-319.e5. https://doi.org/10.1016/j.devcel.2023.01.008

Siebald, C., Vincent, P.F.Y., Bottom, R.T., Sun, S., Reijntjes, D.O.J., Manca, M., Glowatzki, E., Müller, U., 2023. Molecular signatures define subtypes of auditory afferents with distinct peripheral projection patterns and physiological properties. Proc Natl Acad Sci U S A 120, e2217033120. https://doi.org/10.1073/pnas.2217033120

Spoendlin, H., 1985. Anatomy of Cochlear Innervation. American Journal of Otolaryngology 6, 453–467. https://doi.org/10.1016/S0196-0709(85)80026-0

Suda, N., Itoh, T., Nakato, R., Shirakawa, D., Bando, M., Katou, Y., Kataoka, K., Shirahige, K., Tickle, C., Tanaka, M., 2014. Dimeric combinations of MafB, cFos and cJun control the apoptosis-survival balance in limb morphogenesis. Development 141, 2885–2894. https://doi.org/10.1242/dev.099150

Sun, S., Babola, T., Pregernig, G., So, K.S., Nguyen, M., Su, S.-S.M., Palermo, A.T., Bergles, D.E., Burns, J.C., Müller, U., 2018. Hair Cell Mechanotransduction Regulates Spontaneous Activity and Spiral Ganglion Subtype Specification in the Auditory System. Cell 174, 1247-1263.e15. https://doi.org/10.1016/j.cell.2018.07.008

Wende, H., Lechner, S.G., Cheret, C., Bourane, S., Kolanczyk, M.E., Pattyn, A., Reuter, K., Munier, F.L., Carroll, P., Lewin, G.R., Birchmeier, C., 2012. The Transcription Factor c-Maf Controls Touch Receptor Development and Function. Science 335, 1373–1376. https://doi.org/10.1126/science.1214314

Yang, Y., Cvekl, A., 2016. Large Maf Transcription Factors: Cousins of AP-1 Proteins and Important Regulators of Cellular Differentiation. EJBM 23, 2. https://doi.org/10.23861/EJBM20072347

Yin, Y., Liberman, L.D., Maison, S.F., Liberman, M.C., 2014. Olivocochlear Innervation Maintains the Normal Modiolar-Pillar and Habenular-Cuticular Gradients in Cochlear Synaptic Morphology. JARO 15, 571–583. https://doi.org/10.1007/s10162-014-0462-z

Yu, W.-M., Appler, J.M., Kim, Y.-H., Nishitani, A.M., Holt, J.R., Goodrich, L.V., 2013. A Gata3–Mafb transcriptional network directs post-synaptic differentiation in synapses specialized for hearing. eLife 2, e01341. https://doi.org/10.7554/eLife.01341

Yu, W.-M., Goodrich, L.V., 2014. Morphological and physiological development of auditory synapses. Hearing Research 311, 3–16. https://doi.org/10.1016/j.heares.2014.01.007

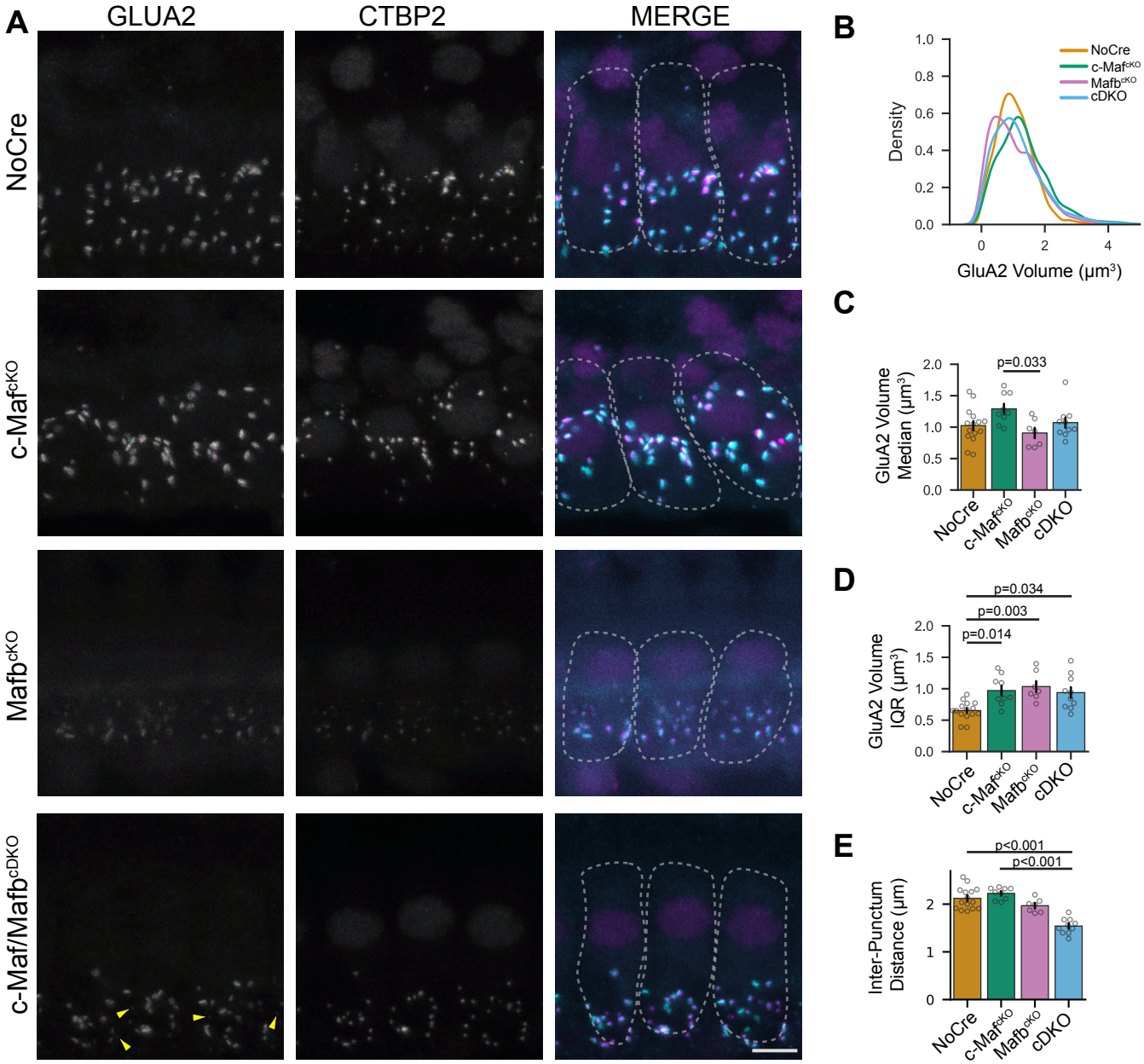
A
GLUA2
CTBP2
MERGE
NoCre
c-Maf^cKO
Mafb^cKO
c-Maf/Mafb^cDKO
B
Density
GluA2 Volume (μm³)
NoCre
c-Maf^cKO
Mafb^cKO
cDKO
C
GluA2 Volume Median (μm³)
p=0.033
D
GluA2 Volume IQR (μm³)
p=0.034
p=0.003
p=0.014
E
Inter-Punctum Distance (μm)
p<0.001
p<0.001

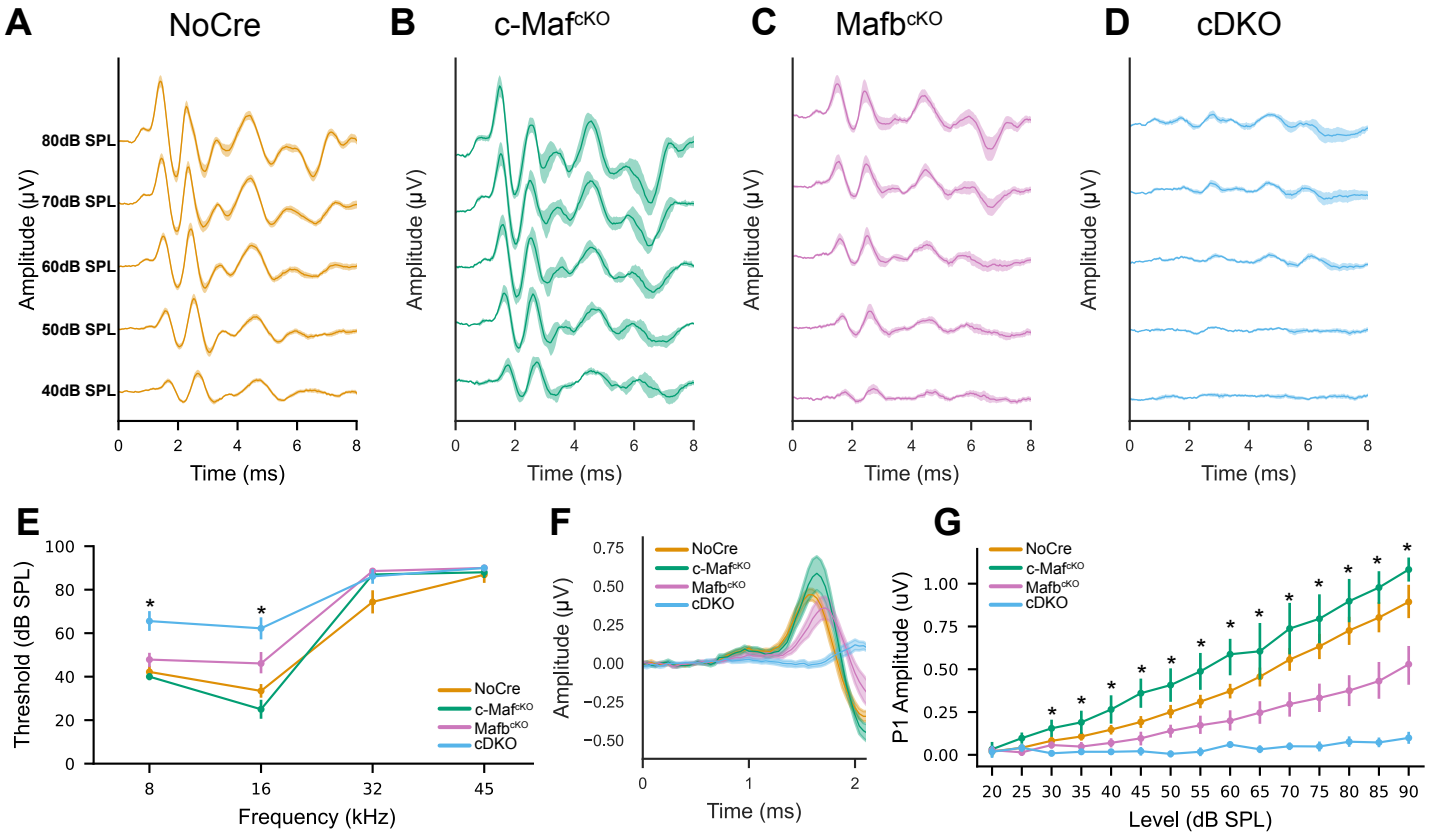
A
NoCre
B
c-Maf^{cKO}
C
Mafb^{cKO}
D
cDKO
80dB SPL
70dB SPL
60dB SPL
50dB SPL
40dB SPL
Amplitude (μV)
Time (ms)
E
Threshold (dB SPL)
Frequency (kHz)
NoCre
c-Maf^{cKO}
Mafb^{cKO}
cDKO
F
Amplitude (μV)
Time (ms)
G
P1 Amplitude (uV)
Level (dB SPL)

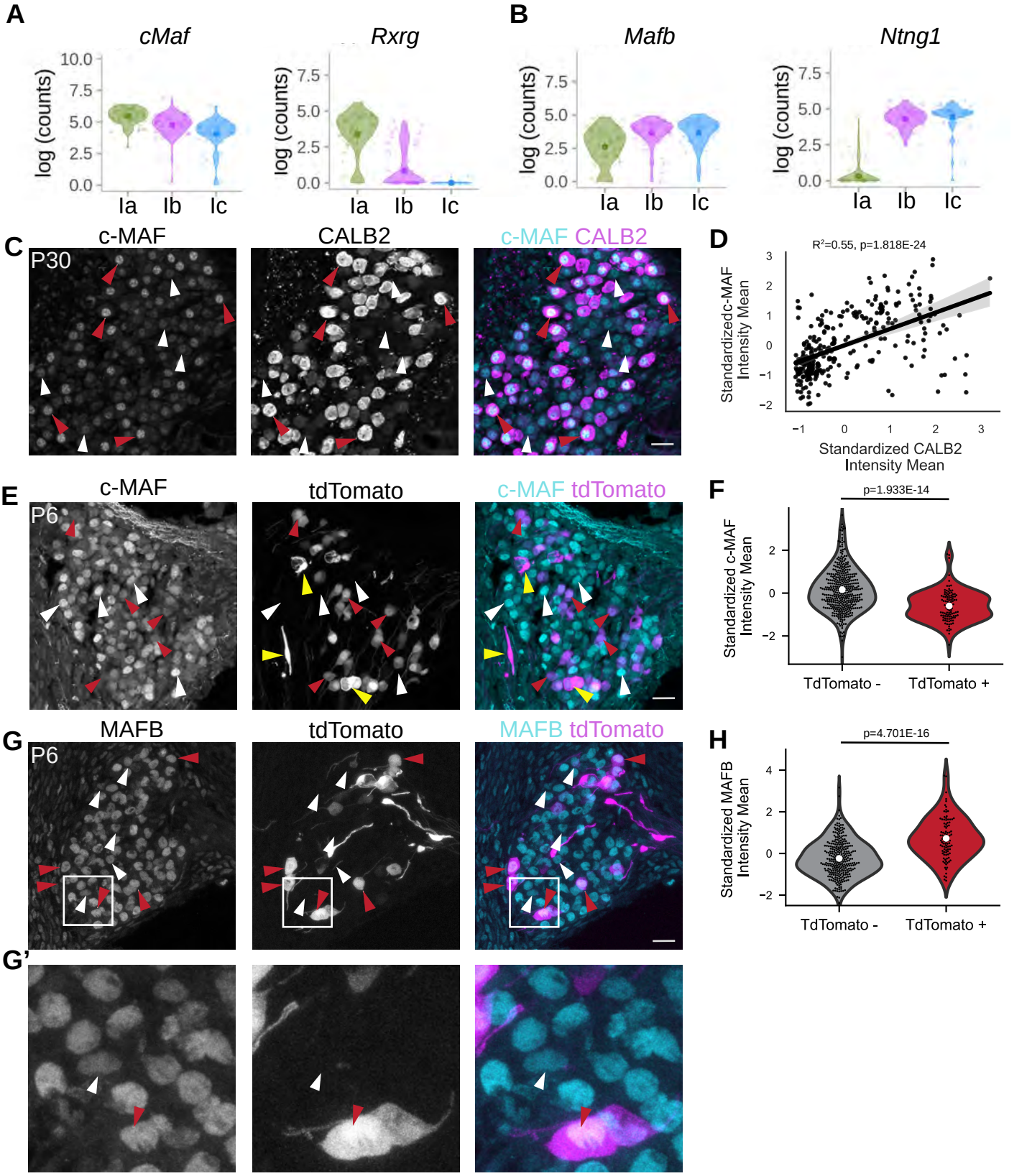
A
cMaf
Rxrg
log (counts)
Ia
Ib
Ic
B
Mafb
Ntng1
C
P30
c-MAF
CALB2
c-MAF CALB2
D
R²=0.55, p=1.818E-24
Standardizedc-MAF Intensity Mean
Standardized CALB2 Intensity Mean
E
P6
c-MAF
tdTomato
c-MAF tdTomato
F
p=1.933E-14
Standardized c-MAF Intensity Mean
TdTomato -
TdTomato +
G
P6
MAFB
tdTomato
MAFB tdTomato
G'
H
p=4.701E-16
Standardized MAFB Intensity Mean

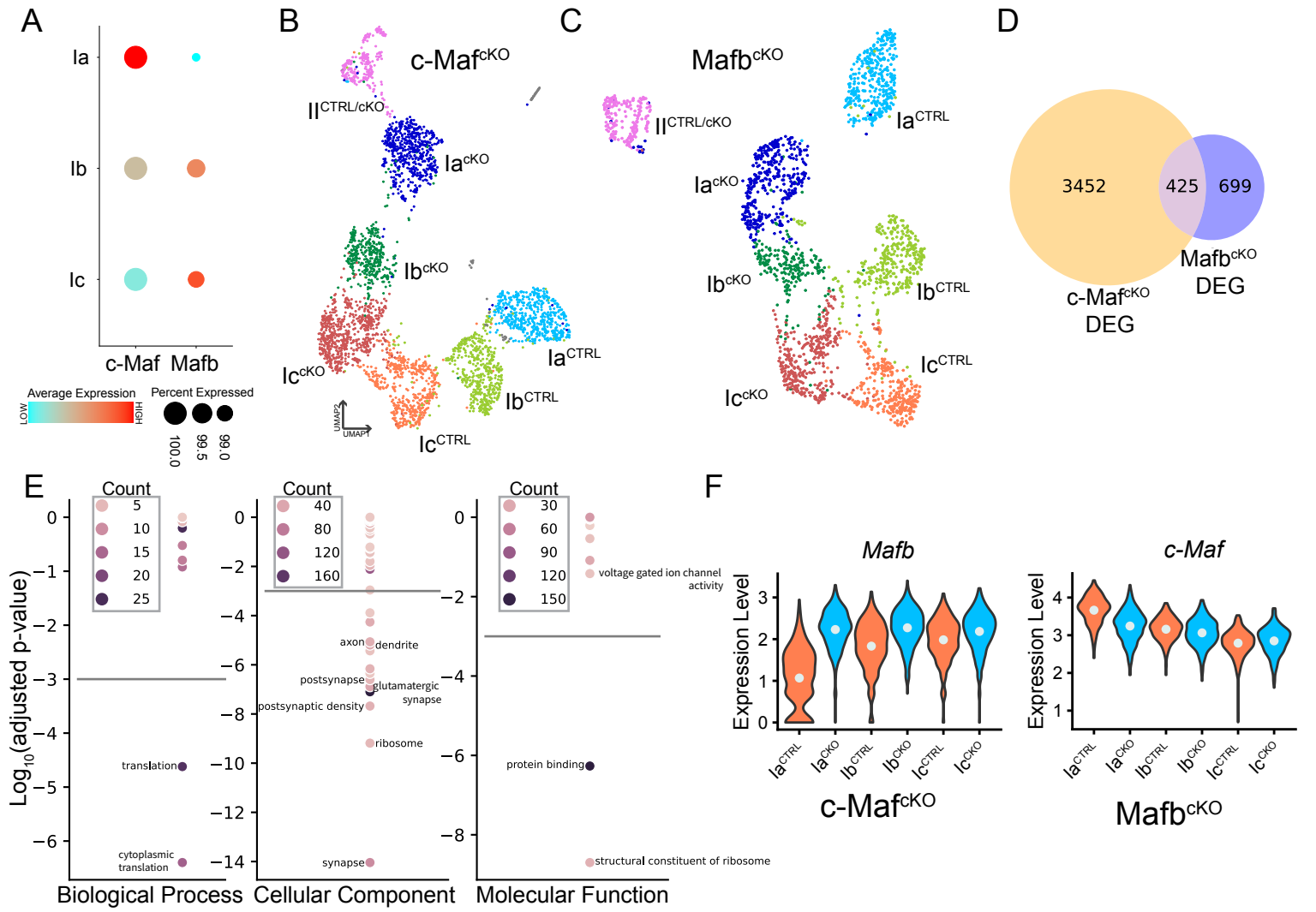
A
Ia
Ib
Ic
c-Maf
Mafb
Average Expression
LOW
HIGH
Percent Expressed
100.0
99.5
99.0
B
c-Maf^{cKO}
II$^{CTRL/cKO}$
Ia^{cKO}
Ib^{cKO}
Ic^{cKO}
Ia^{CTRL}
Ib^{CTRL}
Ic^{CTRL}
UMAP2
UMAP1
C
Mafb^{cKO}
II$^{CTRL/cKO}$
Ia^{CTRL}
Ia^{cKO}
Ib^{cKO}
Ib^{CTRL}
Ic^{CTRL}
Ic^{cKO}
D
3452
425
699
c-Maf^{cKO} DEG
Mafb^{cKO} DEG
E
Count
5
10
15
20
25
translation
cytoplasmic translation
Biological Process
Count
40
80
120
160
axon
dendrite
postsynapse
glutamatergic synapse
postsynaptic density
ribosome
synapse
Cellular Component
Count
30
60
90
120
150
voltage gated ion channel activity
protein binding
structural constituent of ribosome
Molecular Function
Log$_{10}$(adjusted p-value)
F
Mafb
c-Maf
Expression Level
Ia^{CTRL}
Ia^{CKO}
Ib^{CTRL}
Ib^{CKO}
Ic^{CTRL}
Ic^{CKO}
c-Maf^{cKO}
Mafb^{cKO}

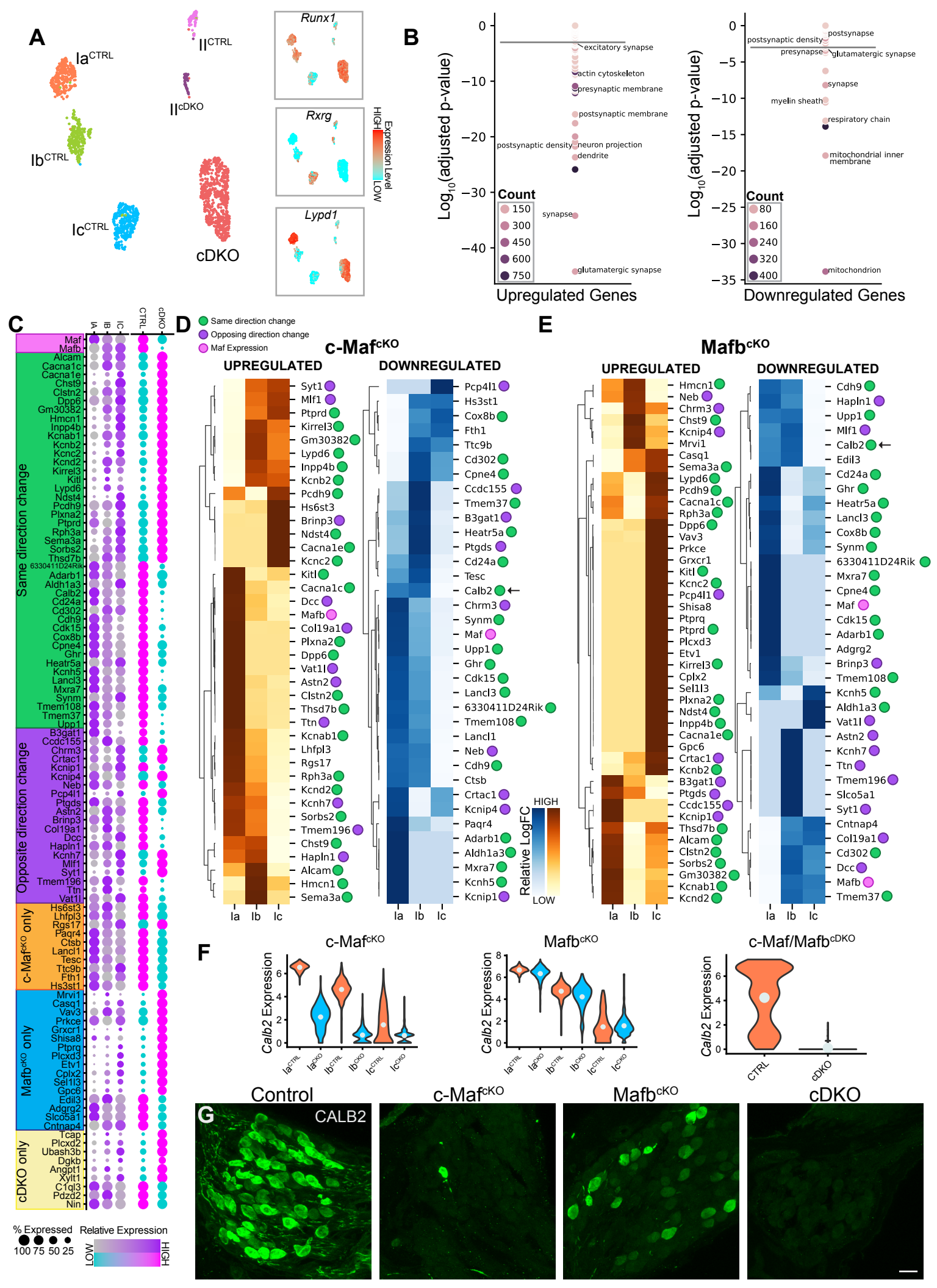
A
Ia^CTRL
Ib^CTRL
Ic^CTRL
II^CTRL
II^cDKO
cDKO
Runx1
Rxrg
Lypd1
HIGH
Expression Level
LOW
B
Log10(adjusted p-value)
excitatory synapse
actin cytoskeleton
presynaptic membrane
postsynaptic membrane
postsynaptic density
neuron projection
dendrite
synapse
glutamatergic synapse
Count
150
300
450
600
750
Upregulated Genes
postsynaptic density
postsynapse
presynapse
glutamatergic synapse
synapse
myelin sheath
respiratory chain
mitochondrial inner membrane
mitochondrion
Count
80
160
240
320
400
Downregulated Genes
C
IA
IB
IC
CTRL
cDKO
Same direction change
Opposite direction change
c-Maf^cKO only
Mafb^cKO only
cDKO only
% Expressed
100 75 50 25
Relative Expression
LOW
HIGH
D
Same direction change
Opposing direction change
Maf Expression
c-Maf^cKO
UPREGULATED
DOWNREGULATED
Relative LogFC
HIGH
LOW
E
Mafb^cKO
UPREGULATED
DOWNREGULATED
F
c-Maf^cKO
Mafb^cKO
c-Maf/Mafb^cDKO
Calb2 Expression
CTRL
cDKO
G
Control
c-Maf^cKO
Mafb^cKO
cDKO
CALB2